OPEN ACCESS

Structural Mechanics Analysis of Woven Web Reinforced Membranes in Proton Exchange Membrane Water Electrolysis

To cite this article: Julian Kink *et al* 2023 *J. Electrochem. Soc.* **170** 114513

Journal of The Electrochemical Society, 2023 **170** 114513

Structural Mechanics Analysis of Woven Web Reinforced Membranes in Proton Exchange Membrane Water Electrolysis

Julian Kink,[1,2,z] Martin Ise,[1] Boris Bensmann,[2] Philipp Junker,[3] and Richard Hanke-Rauschenbach[2]

[1]*Siemens Energy Global GmbH & Co. KG, 91058 Erlangen, Germany*
[2]*Leibniz University Hannover, Institute of Electric Power Systems, 30167 Hannover, Germany*
[3]*Leibniz University Hannover, Institute of Continuum Mechanics, 30823 Garbsen, Germany*

Membranes are a key component of proton exchange membrane water electrolysis (PEMWE) cells and are exposed to various stressors during operation, which can significantly reduce cell lifetime. PEMWE membranes incorporating woven web layers within the membrane structure for mechanical reinforcement are a promising, commonly used industrial strategy to mitigate the formation of membrane defects. Within this study the structural mechanics of a PEMWE cell is investigated, specifically the woven web reinforced membrane. Experimental tensile tests are conducted on the membrane to obtain stress-strain data. These measurements were utilized to parameterize a geometrically simplified model of the woven web reinforced membrane through a tensile test simulation. The validated model is applied in a 2D-cell simulation to identify resulting stresses and strains in the membrane during various electrolysis operation modes. The results herein allow the used PEMWE cell geometry to be systematically evaluated and optimized with respect to mechanical membrane stability. For the applied PEMWE cell setup, no failure is to expect during normal operation, including varied temperatures and differential pressure. Increasing the gap size at the edge of the electrochemically active cell area, however, leads to large deformations when the gap becomes larger than 0.2 mm.
 [DOI: 10.1149/1945-7111/ad0663]

Manuscript submitted July 21, 2023; revised manuscript received October 13, 2023. Published November 10, 2023.

Symbols

$\dot{\varepsilon}_p$	Plastic strain rate
$\dot{\varepsilon}_{pe}$	Equivalent plastic strain rate
C_{mat_iso}	Isotropic elasticity tensor
C_{mat_ortho}	Orthotropic elasticity tensor
E_{iso}	Hardening modulus
E_{Tiso}	Isotropic tangent modulus
F_{el}	Elastic deformation gradient
F_{inel}	Inelastic deformation gradient
$I_{a,i}$	First invariant of the isochoric right Cauchy Green tensor
L_0	Initial length
Q_p	Plastic potential
$S_{PK,el}$	Elastic second Piola-Kirchhoff stress tensor
S_{PK}	Second Piola-Kirchhoff stress tensor
V_f	Fiber volume
V_{sf}	Single-fiber volume
$W_{fib,i}$	Anisotropic strain energy density
$W_{s,el}$	Elastic strain energy density
$W_{s,iso}$	Isotropic strain energy density
W_s	Strain energy density
a_i	Direction vector
d_{mem}	Membrane thickness
g_{size}	Gap size
k_{1x}	Stiffness in x-direction
k_{1y}	Stiffness in y-direction
k_{1z}	Stiffness in z-direction
$\vec{n}$	Normal direction vector to the surface
$r_{m/g}$	Ratio of membrane thickness to gap size width
$\vec{u}$	Displacement vector
x_{wet}	Water content
β_h	Coefficient of hygroscopic expansion
ε_{el}	Elastic strain
ε_{eng}	Engineering strain
ε_{max}	Maximum strain
ε_{pe}	Equivalent plastic strain
ε_{true}	True strain
σ_{eng}	Engineering stress
σ_{eq}	Equivalent stress
σ_{mises}	Von-mises stress
σ_{true}	True stress
σ_{ys}	Yield stress
σ_{ys0}	Initial yield stress
ΔL	Displacement
μ	Lamé parameter
2D	Two dimensions
A_s	Initial sample cross section
BPP	Bipolar plates
d_f	Fiber diameter
DI-water	Deionized water
d_m	Membrane thickness
E	Young's modulus
E_{GL}	Green-Lagrange strain tensor
E_{H21y}	Young's modulus of H_2-PTL 1 in y-direction
E_{O2y}	Young's modulus of O_2-PTL in y-direction
ePTFE	Expanded polytetrafluoroethylene
Eq.	Equation
Eqs.	Equations
E_y	Young's modulus in y-direction
F	Deformation gradient
F_T	Tensile force
F_y	Yield criterion
G	Shear modulus
g_{size}	Gap size width
H_2	Hydrogen
I_1	First invariant of the strain tensor
J_2S	Second invariant of the stress tensor
J_{el}	Elastic volume ratio
$k_{1,i}$	Stiffness in i-direction
k_2	Fitting parameter
k_3	Fiber distribution
L	Side length
MEA	Membrane electrode assembly
n	Number
O_2	Oxygen
p	Pressure

[z]E-mail: julian.kink@siemens-energy.com

PEEK	Polyetheretherketone
PEMWE	Proton exchange membrane water electrolysis
p_{H_2}	Pressure on H_2 side
p_{O_2}	Pressure on O_2 side
PTL	Porous transport layer
Q_i	Exponent for the calculation of $W_{fib,i}$
Q_P	Plastic potential
RH	Room humidity
SED	Strain energy density
s_f	Fiber-to-fiber distance
T	Temperature
t_k	Current timestep
v	Displacement in y-direction
V	Volume
α	Coefficient of thermal expansion
ε_y	Strain in y-direction
λ	Lamé parameter
λ_p	Plastic multiplier
ν	Poisson's ratio

This study focuses on the mechanical characterization of a woven web reinforced membrane and its mechanical behavior within a proton exchange membrane water electrolysis (PEMWE) cell setup. PEMWE technology plays an essential role in the field of green hydrogen production, alongside alkaline water electrolysis, anion exchange water electrolysis and solid oxide water electrolysis.[1] The membrane is a key component within the electrolysis cell, separating the electrodes and the produced gases.[2] However, the membrane is subjected to various loads in the PEMWE cell, ranging from temperature effects, chemical interactions with the environment, and mechanical stress. Here we focus on the mechanical impact on the membrane and the resulting deformations that can lead to cracks, pinholes, and membrane thinning. Such failures have been extensively investigated in the related PEM fuel cell community[3–9] and are recently shown to be an issue for PEM water electrolysis as well.[10,11]

Decreasing the possibility of such damages can be achieved by reducing the mechanical stresses or by using thicker membranes. In the recent years, commercially available options for reinforcing the membrane mechanically have emerged, offering an effective possibility to prevent membrane damages.[2,12] In addition to enhancing the mechanical robustness of the membrane, membrane reinforcement leads to an optimized dimensional stability by reducing in-plane swelling.[2,13,14] Furthermore, the reinforcement improves the handling of the membrane because of the higher mechanical stiffness.

There are several technologies for the membrane reinforcement, for instance ePTFE (expanded PTFE),[2,12,15–17] nanofibers,[18–20] and woven web.[2,12] Main technologies, which are commercially available, are ePTFE[13,14] and woven web[12] reinforcements. For PEM fuel cells, the ePTFE reinforced membranes are experimentally well investigated[2,12,15–17] and two modeling approaches are presented.[13,14] A gap in the open literature is the investigation of membranes reinforced by woven web. To the best of our knowledge there are no experimental investigations and no modeling data available. Additionally, a fundamental investigation on the mechanical effect of the reinforcement of a membrane inside the PEMWE cell is not available.

In this paper, a simplified simulation of a PEMWE cell setup using the reinforced fumasep® FS-990-PK membrane is presented. For the membrane, a simplified model with a substitute geometry for the reinforcement layer is used. The parameterization of the model is performed using experimental data from tensile tests which are carried out for this purpose. With this, the cell simulation can be executed out and the mechanical response of the membrane during the assembly process and operation are calculated. Next, a parameter study follows regarding variation of differential pressure across the membrane (pressure difference between O_2 and H_2 side: $\Delta p = p_{O_2} - p_{H_2}$), cell pressure variation, temperature variation, and gap width variation. Additionally, the influence of the reinforcement is investigated and thereafter, the results are compared to a simulation without reinforcement.

The paper is structured as follows: first, the geometry of the PEMWE cell is presented, and simplifications are made for the simulation model. In the subsequent chapter, a substitute geometry for the reinforced membrane is introduced. Additionally, the experimental tensile tests are explained, and their use for the parameterization and validation of the membrane material model is described. Next, the results of the PEMWE cell simulation, employing the material model of the membrane, are presented along with various parametric studies. Finally, a summary of the results is provided, followed by an outlook on future work.

2D-Model of the PEMWE Cell

At the beginning of this section, the geometry of the investigated PEMWE cell setup is presented. Subsequently, the modeling approach with the required simplifications is described. The applied boundary conditions for the simulation are given afterwards, followed by the material models used. Last, the assembly steps and load cases which are simulated, including the parametric studies, are shown.

Geometry of the investigated PEMWE cell setup.—A representative and up to date PEMWE cell setup is depicted in Fig. 1A, showcasing a cross-sectional view. The cell's geometric outline is based on a recent patent from Siemens Energy.[21] The Membrane Electrode Assembly (MEA) is situated in the center, comprising the membrane and catalyst layers on both sides serving as electrodes. In the present study, the catalyst layers are neglected as it is expected that their influence on the mechanical stability of the membrane is small. This assumption is commonly made in PEMWE[11] and PEM fuel cell[7,11,22–24] simulations. The membrane employed is the woven web reinforced fumasep® FS-990-PK, manufactured by FUMATECH, with a thickness of 90 μm in a dry state. The reinforcement material within the membrane consists of non-ion conductive polyetheretherketone (PEEK) woven fibers. The matrix of the material is an ion-conductive ionomer. On the top and the bottom of the MEA, the H_2 and O_2-PTLs are located, with varying dimensions. Hence, the surrounding frame has a stepped geometry and the O_2-PTL lies on this step. The H_2-PTL is divided in two layers, one with high compressibility and the other with low compressibility. The top and the bottom of the cell is sealed by the bipolar plates (BPP), closing the cell, and marking the beginning of the following cell. The sealings are neglected in the present investigation.

Figure 1B illustrates the compressed cell after assembly and compression. The compression is achieved by pressing the BPP onto the cell frame, resulting in the compression of the PTLs. Consequently, the PTLs are pressed on the membrane.

For modeling purposes, the geometry needs to be simplified (Fig. 1C). Due to limited computational power, only a small region of the cell can be simulated. Consequently, the simulated cell is assumed to be smaller than typical commercial PEMWE cells in x-dimension. This approach is valid since the components near the transition zone between cell frame and H_2-PTL are of particular interest. This area is critical as it represents a potential point of membrane failure.[6,9,11] The reason for that is, that a gap cannot be avoided and therefore the membrane has no support in this area. Additionally, the bipolar plates are neglected, and the compression is applied directly on the cell frame and the PTLs.

Modeling approach.—The modeling framework is based on the finite element method[25] and the software COMSOL Multiphysics®[26] is used. For the model, a 2D plane strain simplification is used with a transient solver. Quasistatic behavior is assumed, and implicit time

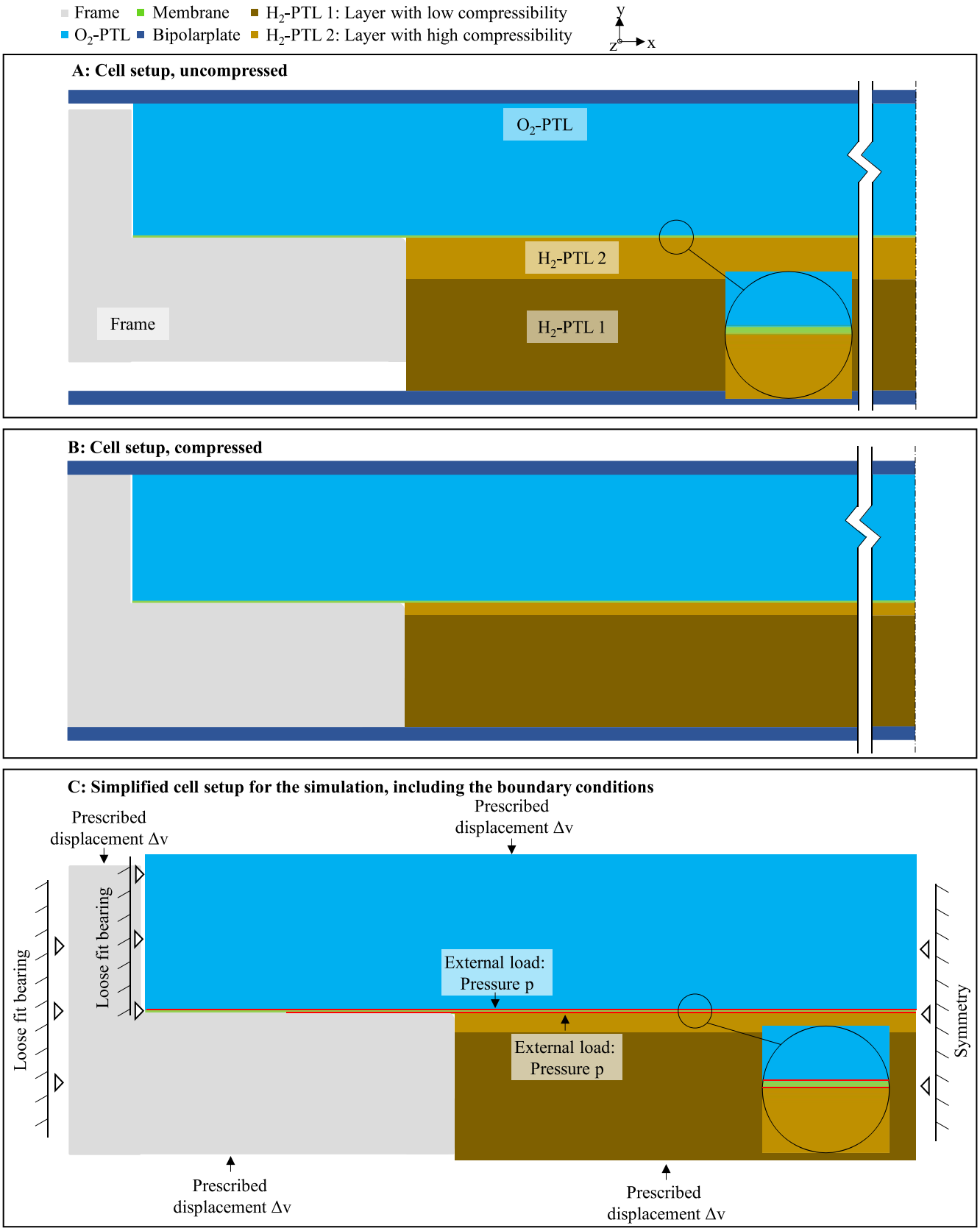

Figure 1. Schematic illustration of the cross-section of a proton exchange membrane electrolyzer cell: uncompressed (A), compressed (B), simplified setup for simulation with boundary conditions (C).

integration applied. The meshing is performed using triangle and square elements summing up to a total of 177,515 elements. The discretization is done with a quadratic serendipity shape function.

The model applies large deformation for the materials with low stiffness (Membrane, H_2-PTL 2) and is based on multiplicative split of the deformation gradient F (Eq. 1), where the inelastic

deformation gradient is defined in Eq. 2.

$$F = F_{\text{el}} F_{\text{inel}} \quad [1]$$

$$F_{\text{inel}} = \prod F_{\text{inel},i} \quad [2]$$

The governing equations for structural mechanics can be found in our recent publication[11] (Eqs. 1–7), and in a similar manner in the appendix. For the clarity and readability of the present paper, they are not repeated here.

Boundary conditions and applied load cases in the electrolyzer simulation.—A loose fit bearing is used on the left side of the cell frame, where the displacement vector $\vec{u}$ in the normal direction to the surface $\vec{n}$ (here in x-direction, so $\vec{n} = (1,0,0)$) is constrained to zero (Eq. 3).

$$\vec{u} \cdot \vec{n} = 0 \quad [3]$$

However, this boundary is allowed to move in response to the thermal expansion of the material. This displacement is calculated in advance and implemented directly as prescribed displacement. Considering the compressed cell, the thermal expansion of the cell frame in x-direction is constrained by the bipolar plate due to the high friction on its top and the bottom surfaces. Therefore, it is assumed that the expansion of the left boundary of the cell frame corresponds to the expansion of the bipolar plate.

In the middle of the cell, meaning the right boundary of the model setup in Fig. 1C, a symmetry boundary is applied, which is numerically equal to the loose fit bearing in Eq. 3.

On top and bottom of the cell, a prescribed displacement condition in y-direction ($\vec{n} = (0,1,0)$) is applied on the boundaries. This causes the cell to be compressed. The pressure p is applied as an external load (Eq. 4) directly on the membrane, as indicated in Fig. 1C. S_{PK} stands for the second Piola-Kirchhoff stress tensor.

$$S_{\text{PK}} \vec{n} = -p \quad \vec{n} \quad [4]$$

The simulation uses penalty-based contacts. To simplify the model, the contact between H_2-PTL 1 and H_2-PTL 2 is defined as an identity pair, indicating that their boundaries are a permanent, fixed pair. Similarly, the layered membrane, which will be discussed in the next section, also uses an identity pair for contact definition. The contact between cell frame and H_2-PTL is assumed to be without friction. The other contacts are using the Coulomb friction law. Specifically, the friction coefficient between O_2-PTL and the membrane is set to 0.5 (conducted in friction measurements according to DIN EN ISO 8295), while the friction coefficients between H_2-PTL 2 and the membrane, as well as between cell frame and the membrane, are both set to 0.2. These friction coefficients are not measured but assumed to be lower than the friction coefficient between O_2-PTL and the membrane because of their smoother surface.

Material models used.—The cell frame is defined as linear elastic material with an isotropic elasticity tensor $C_{mat\_iso} = C_{mat\_iso}(E, \nu)$, which is a valid approach as the deformations are expected to be small. The elasticity tensor is composed of material data E, the Young's modulus and ν, the Poisson's ratio. The stress tensor σ is calculated with Eq. 5, where ε_{el} is the elastic strain.

$$\sigma = C_{\text{mat\_iso}} : \varepsilon_{\text{el}} \quad [5]$$

O_2-PTL and H_2-PTL 1 are both assumed to be homogeneous and modeled orthotropic-elastic. This choice is justified by the expectation of small deformations. The material data are conducted from pressure and bending tests, from which the Young's modulus $E = E(x, y, z)$, the Poisson's ratio $\nu = \nu(x, y, z)$, and the shear modulus $G = G(x, y, z)$ can be determined. The calculation is done with Eq. 5 as well and the elasticity tensor is defined as $C_{\text{mat\_ortho}} = C_{\text{mat\_ortho}}(E, \nu, G)$. In x and z-direction we assume a constant Young's modulus E_x and E_z. In y-direction, the stress-strain characteristics is nonlinear, which we account for by choosing $E_y = E_y(\varepsilon)$ and thus $C_{\text{mat\_ortho}} = C_{\text{mat\_ortho}}(\varepsilon)$.

The H_2-PTL 2 is assumed as highly compressible material which can be calculated with Eq. 5. The material parameters used for the parts described above can be found in Table I.

The woven web membrane cannot be simulated in 2D without proper simplifications because there is no distinct 2D-section resulting from its geometry. Therefore, as already indicated, in the following chapter, a homogenized middle layer is introduced, which represents the woven web.

Model of the Woven Web Reinforced Membrane and its Parametrization Based on Experimental Tensile Tests

In this chapter, the geometry of the used membrane FS-990-PK is described. Subsequently, a simplified geometric model for the woven web reinforcement within the membrane is proposed. Afterwards, experimental tensile tests are performed with the membrane and the results are presented. Using these data, appropriate material models are chosen for the electrolyzer simulation and necessary material constants are determined.

Geometric dimensions of the membrane and its simplifications for the simulation.—The fumasep® FS-990-PK membrane by FUMATECH is a composite membrane composed of a woven web consisting of fibers and an ionomer (or named functional polymer) as a matrix. The fibers of the woven web have a diameter of $d_f = 30\ \mu$m and a fiber-to-fiber distance of $s_f = 200\ \mu$m. A cross sectional view can be found in the book of Scott[12] and microscopic pictures are shown in the appendix in Fig. A·1. Additionally, a schematic of the membrane is depicted in the appendix in Fig. A·2. The thickness of the dry membrane is 90 μm.

To have a simplified, but representative 2D-section of the membrane, a homogeneous middle layer is introduced (Fig. 2, zoom towards the membrane in Fig. 1). The layer represents the woven web membrane. Its thickness is determined from the volumetric part of the woven web in one direction of the two fiber directions. Assuming a membrane square with the side length L, the volume V_{sf} of a single fiber is $V_{\text{sf}} = \left(\frac{d_f}{2}\right)^2 * \pi * L$. In one of the in-plane directions, there are $n = \frac{L}{s_f + d_f}$ fibers. This leads to the volume of n fibers in one in-plane direction of $V_f = n * V_{\text{sf}} = \left(\frac{d_f}{2}\right)^2 * \pi * \frac{L^2}{s_f + d_f} = 3.07\ \mu\text{m} * L^2$. This means that the volume of the fibers oriented in the same direction is $3.07\ \mu\text{m} * L^2$ and therefore the thickness of the middle layer in the membrane is defined as 3.07 μm.

The other two layers of the membrane, as it can be seen in Fig. 2, are the functional polymer parts, each with a thickness of 43.23 μm.

For choosing an appropriate material model, experimental data are required. Hence, in the next part, experimental tensile tests are discussed.

Experimental data acquisition with tensile tests.—The tensile behavior of the membrane can be determined by tensile measurements according to DIN EN ISO 527–1[27] with a minimum of three repetitions. These tests provide force-displacement data which can be calculated into stress-strain data, allowing for the characterization of the membrane's mechanical properties. The testing involves the commercially available membrane fumasep® FS-990-PK (Fig. A·1 *left*) as well as the reinforcement woven web (Fig. A·1 *right*). The reinforcement material used in the membrane is PEEK, and it is consistently referred to as such in all figures.

Before using the materials, they were conditioned in an air-conditioned cabinet at a temperature $T = 23$ °C and room humidity

Table I. Material parameters used for cell frame and PTLs.

	Cell frame	O_2-PTL	H_2-PTL 1	H_2-PTL 2
Young's-modulus E	11.9 GPa	$(E_x, E_y, E_z) = (1.09, E_{O2y}$[a)]$, 0.69)$ GPa	$(E_x, E_y, E_z) = (11.27, E_{H21y}$[a)]$, 5.72)$ GPa	4.07 MPa
Poisson's ratio ν	0.39	10^{-6}	10^{-6}	10^{-4}
Shear modulus G	—	15.94 GPa	36.22 GPa	—
Coefficient of thermal expansion α	4[a)]10^{-5} K^{-1}	8.7[a)]10^{-6} K^{-1}	1.65[a)]10^{-5} K^{-1}	2.4[a)]10^{-6} K^{-1}

a) E_{O2y} and E_{H21y} are referring to nonlinear Young's moduli ranging from 1.6–62 MPa and 1.7–22 MPa, depending on the compression in y-direction ε_y (determined in pressure tests).

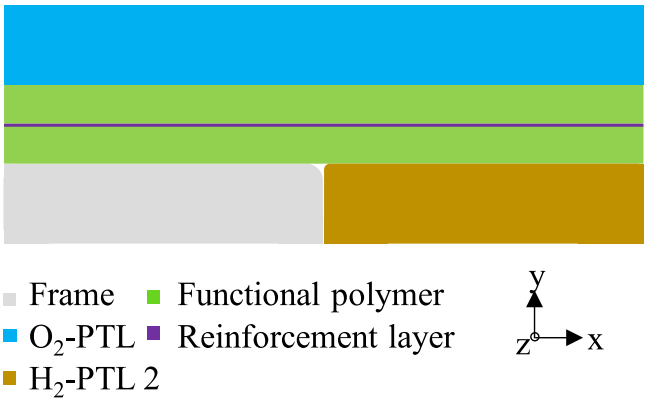

Figure 2. Geometric outline of the reinforcement layer used in the simulation setup (zoom of Fig. 1).

RH = 30% for at least 24 h. For testing wet samples, the material was stored in a water tank placed in the cabinet. The outline of the samples follow DIN EN ISO 527–3,[28] probe body type 2, and were cut with a punch. The dimensions are given in Fig. A·3, 100 mm for dry samples and 130 mm for wet samples. As testing machine, the Z010 from ZwickRoell GmbH & Co. KG was used in the same setup as in a previous publication[11] (Fig. A·3).

The force-displacement data obtained from wet samples using the water tank requires correction due to density differences between water and air, resulting in a shift in the results. To compensate this error, a correction curve is determined with a tensile test without clamped sample. These corrected results are depicted in Fig. 3A.

Figure 3A demonstrates that the mechanical stiffness decreases with increasing temperature and with increasing water content within both the membrane FS-990-PK and within the reinforcement material, PEEK. This is a known effect which is common, especially for ionomers.[2] Comparing the curves of the membrane and PEEK it is evident that the influence of the reinforcement layer is significant as the measured forces at a defined strain are always at least 50% of the forces observed for the membrane.

To facilitate further analysis, the data needs to be converted into engineering stress (σ_{eng})—engineering strain (ε_{eng}) curves. The engineering stress is defined as $\sigma_{eng} = \frac{F_T}{A_S}$, while the engineering strain is calculated as $\varepsilon_{eng} = \frac{\Delta L}{L_0}$, with F_T the tensile force, A_S the area of the initial sample cross section, ΔL the displacement and L_0 the initial length of the sample. It is important to note that the calculation of the engineering stress-strain data assumes a constant cross-sectional area A_S, which means material thinning is not considered. For receiving true stress (σ_{true})—true strain (ε_{true}) curves, Eqs. 6 and 7 are used as an approximation for conversion.[29,30]

$$\varepsilon_{true} = \ln\,(1 + \varepsilon_{eng}) \quad [6]$$

$$\sigma_{true} = \sigma_{eng}(1 + \varepsilon_{eng}) \quad [7]$$

These calculations lead to the true stress-true strain curves in Fig. 3B (reinforcement) and Fig. 3C (membrane). Similar to the force-displacement data, these curves highlight the dependence of the mechanical behavior on temperature and water content. The reinforcement layer has at the beginning a nearly linear elastic behavior, followed by a decreasing slope of the stress. This indicates a transition from elastic to plastic deformation.

The results in the membrane show a similar response, but with stress values approximately one magnitude lower than those of the reinforcement. This is to be expected due to the different Young's modulus of the material, differing by approximately a factor of 10^2.[31] Additionally, the transition zone from elasticity to plasticity is

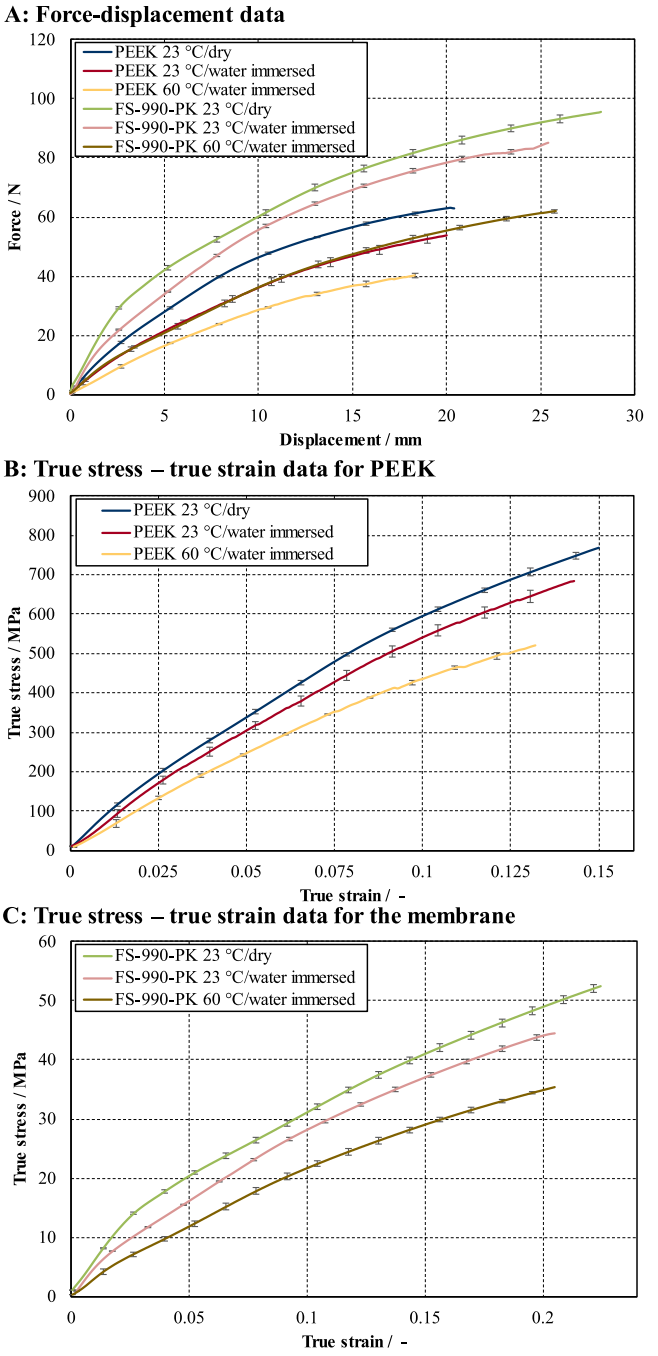

Figure 3. Tensile test results for the reinforced membrane (FS-990-PK) and the reinforcement woven web (PEEK). A: Force-displacement data and B, C: True stress-true strain data.

more evident in the membrane, as the slope of the stress changes more rapidly following the initial elastic deformation.

Membrane material models and tensile test simulations.— Using the simplified geometry of the membrane presented in Fig. 2, it is necessary to define appropriate material models and parameterize them using the experimental tensile test data in Fig. 3. Since the deformations of the membrane and the reinforcement layer are large ($\varepsilon_{max} >> 0.05$), the material models need to be hyperelastic. Additionally, the material models need to calculate the plastic behavior as well. For the parameterization of the models, simulations of tensile tests must be performed. In Fig. 4, the used tensile simulation model setup is illustrated. On the bottom edge, the

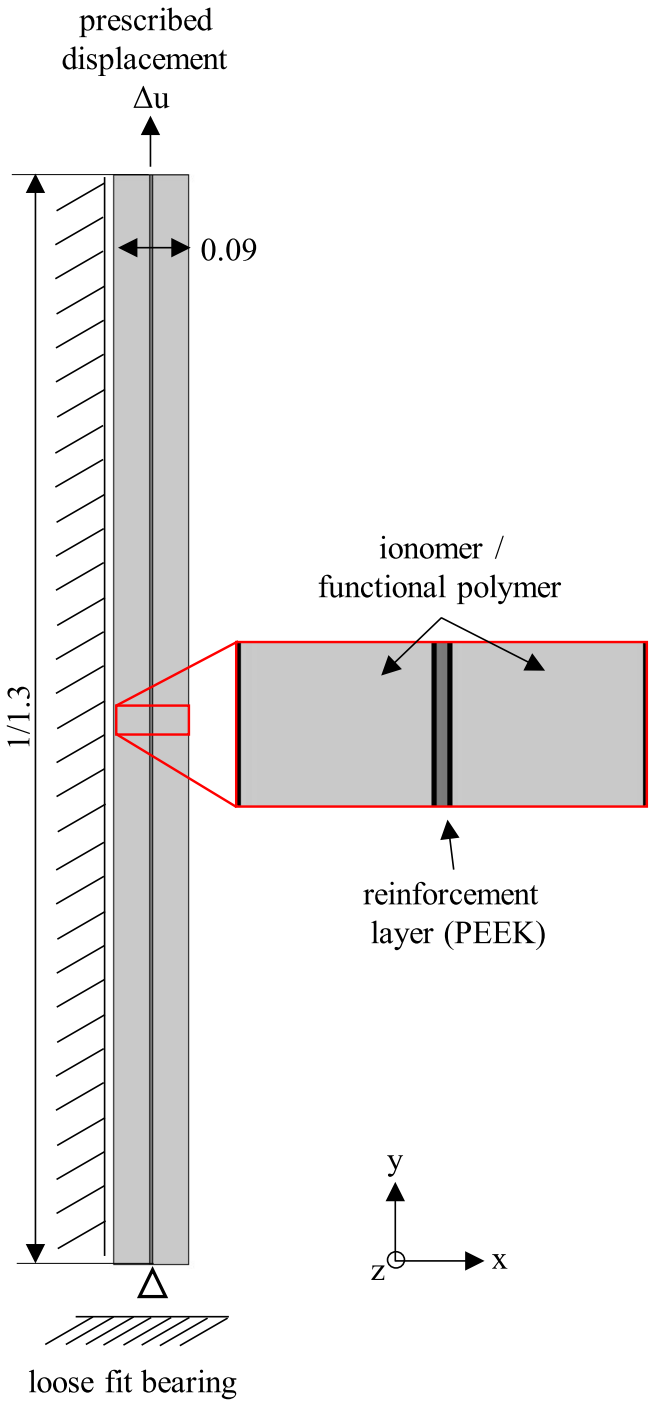

Figure 4. Tensile test simulation setup with the simplified geometry of the membrane FS-990-PK. The woven mesh is simplified and represented as a homogeneous middle layer. The dimensions are given in mm.

displacement is restricted in y-direction. On the left side edge, the displacement is restricted in x-direction. On the top side, the displacement in y-direction is prescribed. In the middle of the membrane is the reinforcement layer and on the outside the ionomer like in Fig. 2. The length of the sample (y-direction) in the simulation is reduced to 1% of the length in the experimental tensile test, i.e., 1 mm for dry and 1.3 mm for wet tests. The dimensions in x and z-direction are identical to the experiment. The discretization is quadratic serendipity.

For the ionomer part of the membrane, an isotropic hyperelastic Neo-Hookean material model is applied. This material model postulates the strain energy density W_s, also called elastic potential, by Eq. 8 from which the second Piola-Kirchhoff stress tensor is derived in usual manner in Eq. 9.[32] The model uses the Lamé parameters μ and λ, which can be calculated from the Young's modulus and Poisson's ratio.[25] The Young's modulus is determined in the three different experimental setups (dry 23 °C, wet 23 °C, wet 60 °C) and interpolated inbetween. The Poisson's ratio for the ionomer is assumed to be similar to the one of Nafion®.[33] $I_1 = \mathrm{trace}(C_{el})$ stands for the first invariant of the elastic right Cauchy-Green strain tensor.

$$W_{s,el} = 0.5 * \mu * \quad (I_1 - 3) - \mu * \quad \ln(J_{el}) + 0.5 * \quad \lambda * \quad (\ln(J_{el}))^2 \qquad [8]$$

$$S_{PK,el} = 2\frac{\partial W_{s,el}}{\partial C_{el}} \qquad [9]$$

The plastic potential Q_p is calculated with Eq. 10. It is equal to the von-Mises stress, which is here defined using the second invariant of the stress tensor $J_2(\sigma) = \frac{1}{2} \quad * \quad (\mathrm{trace}(\sigma)^2 - \mathrm{trace}(\sigma^2))$.

$$Q_p = \sigma_{mises} = \sqrt{3J_2(\sigma)} \qquad [10]$$

When the deformations exceed a certain stress level, the plastic deformation begins. This means, the deformation is permanent and after the load is released the (plastic) deformation stays. The beginning of the plastic region is marked by the yield stress σ_{ys}, which is calculated based on the initial yield stress σ_{ys0}, where usually a change of the slope in the stress-strain curve can be observed. During plastic deformation, the yield stress rises according to the linear hardening function in Eq. 11. E_{iso} is calculated from with $E_{iso}^{-1} = E_{Tiso}^{-1} - E^{-1}$, where E_{Tiso} is the tangent modulus and E the Young's modulus. ε_{pe} is the equivalent plastic strain.

$$\sigma_{ys} = \sigma_{ys0} + E_{iso} \quad * \quad \varepsilon_{pe} \qquad [11]$$

The yield criterion F_y can be calculated using Eq. 12. For $F_y < 0$ the deformation is elastic, for $F_y > 0$ the deformation is plastic.

$$F_y = \sigma_{eq} - \sigma_{ys} \qquad [12]$$

As equivalent stress σ_{eq} at the current step the von-Mises stress σ_{mises} is used, see Eq. 13.

$$\sigma_{eq} = \sigma_{mises} \qquad [13]$$

The equivalent plastic strain ε_{pe} can be calculated by integrating the equivalent plastic strain rate $\dot{\varepsilon}_{pe}$, which is defined in Eq. 14, using $\mathrm{dev}(\dot{\varepsilon}_p) = \dot{\varepsilon}_p - \frac{1}{3}\mathrm{trace}(\dot{\varepsilon}_p) \quad * \quad I_d$.

$$\dot{\varepsilon}_{pe} = \sqrt{\frac{2}{3}\mathrm{dev}(\dot{\varepsilon}_p) : \mathrm{dev}(\dot{\varepsilon}_p)} \qquad [14]$$

Therefore, the increment of the plastic strain tensor $\dot{\varepsilon}_p$ is needed, which is defined as the derivation of the plastic potential Q_p with respect to the current state of stress σ multiplied with a plastic multiplier λ_p. The plastic multiplier depends on the current state of the stress and the load history, for more details see.[32]

$$\dot{\varepsilon}_p = \lambda_p \frac{\partial Q_p}{\partial \sigma} \qquad [15]$$

The previous statements are intended to give the reader a short introduction in plasticity. It is based on the main formulas used in COMSOL Multiphysics®.[32] For more details and further explanations regarding plasticity and its numerical treatment, see the COMSOL Manual,[32] Betten,[34] Bertram[35] or Dimitrienko.[36] The used material parameters are presented in Table II.

In addition to the plastic deformation, the thermal expansion of the material of the reinforcement layer is considered using Eq. 16. F_{inel} stands for the inelastic deformation gradient and t_k for the current timestep. I_{d} is the identity matrix, α is the coefficient of thermal expansion and T the temperature.

Furthermore, the hygroscopic swelling is calculated with Eq. 17. The coefficient of hygroscopic expansion is referred as β_h and x_{wet} refers to the water content, which is 0 for the dry state (conditioned at T = 23 °C and RH = 30%) and 1 for the membrane being fully saturated in water.

$$F_{\text{inel}}(t_k) = F_{\text{inel}}(t_{k-1}) \quad * \quad I_{\text{d}}[1 + \alpha(T(t_k) - T(t_{k-1}))] \qquad [16]$$

$$F_{\text{inel}}(t_k) = F_{\text{inel}}(t_{k-1}) \quad * \quad I_{\text{d}}[1 + \beta_h(x_{\text{wet}}(t_k) - x_{\text{wet}}(t_{k-1}))] \qquad [17]$$

The swelling behavior of membranes, such as Nafion®, has been extensively studied in the literature.[2,37–39] However, limited information is available regarding the swelling behavior of the fumasep® FS-990-PK membrane, with no specific investigations documented except for the data sheet provided by the producer, FUMATECH. According to the data sheet, the in-plane swelling of the FS-990-PK membrane is reported to be less than 2%.[40]

Hence, several swelling tests were conducted with the FS-990-PK membrane. At first, the dimensions of membrane samples were measured at T = 23 °C and RH = 30%. The samples were placed in DI-water for at least 24 h. Sample 1 was in a cabinet with T = 23 °C and sample 2 with T = 60 °C. Both samples showed an in-plane swelling below 1%. The through-plane swelling of sample 1 was 26.0% whereas sample 2 was 42.7%. Assuming a uniform, isotropic swelling, sample 1 expanded 8.5% in each direction and sample 2 expanded 13.04%. However, the results of the second sample were shifted because of the additional thermal expansion. The thermal expansion can be calculated by using the thermal coefficient and the temperature difference to 0.46%. Subtracting this leads to a corrected swelling expansion of 12.58%.

With the equations above, the ionomer part of the membrane is fully described. Next, a material model for the reinforcement layer is presented. The fibers in the woven web of the reinforcement layer are directed x- and z-direction (perpendicular to the y-direction). Hence, the material needs to be modeled anisotropically. As the ionomer, the material is hyperelastic-plastic, so the stress is calculated according to Eq. 9. The strain energy density is, however, calculated differently due to the anisotropy.

Therefore, the Holzapfel-Gasser-Ogden-Model[32,41–43] is applied. This constitutive material model was invented to capture the anisotropic mechanical response observed in arteries. Arteries consist of several layers, which are supported by two families of collagen fibers. Additionally, the possible deformation of arteries is large and therefore the model is developed to be suitable for large deformations.[41]

Caused by the anisotropy, the strain energy density is decomposed additively into three parts, see (18). The first part $W_{s,iso}$ is an isotropic contribution defined by a Neo-Hooke mode, identical to Eq. 8. The second and third parts $W_{fib,i}$ are the additional contributions for the fibers. The definition is given in Eqs. 19 and 20.

$$W_{\text{s}} = W_{\text{s,iso}} + W_{\text{fib},1} + W_{\text{fib},2} \qquad [18]$$

$$W_{\text{fib},i} = \frac{\text{k}_{1,i}}{2\text{k}_2} \quad * \quad (\exp(Q_i) - 1) \qquad [19]$$

The parameters are defined as follows: $\text{k}_{1,\text{i}}$ is the stiffness in a_i direction and k_2 a fitting parameter. k_3 in Eq. 20 describes the fiber dispersion and is 0 for perfectly oriented fibers in a_i-direction. In the membrane, the fibers are distributed perfectly in x- and z-direction and therefore k_3 is 0. This leads to the simplified formula in Eq. 21. $I_{a,i}$ is invariant with respect to rotation around the a_i-direction that represents the squared value of the isochoric elastic stretch in the fiber direction a_i (x-direction for i = 1 (a_1 = (1,0,0)) and z-direction for i = 2 (a_2 = (0,0,1))).[32]

$$Q_i = k_2(k_3(I_1 - 3) + (1 - 3k_3)(I_{a,i} - 1))^2 \qquad [20]$$

$$Q_i(k_3 = 0) = k_2(I_{a,i} - 1)^2 \qquad [21]$$

The anisotropic material model is established using Eqs. 18 to 21. The parameter k_2 is set equal to 1. To define the material parameters completely, it must be taken into account that the strain energy density contains an isotropic contribution $W_{\text{s,iso}}$ while the other two components $W_{\text{fib},i}$ contribute each in one fiber direction. Therefore, when considering a Young's modulus in the direction a_i, it must be decomposed into two contributions.

In the following simulations, it is assumed that the reinforcement layer has a reduced impact in through-plane direction, so the stiffness in y-direction $k_{1,\text{y}}$, depending only on $W_{\text{s,iso}}$, is assumed to be only 10% of the Young's modulus E. The reason for this is, that there are no fibers in this direction. Because of the definition of $W_{\text{s,iso}}$, there is already a stiffness of 10%*E in each direction (x, y, z), thus only 90% need to be added at each fiber contribution $W_{\text{fib},i}$ (for x and z-direction). Hence, the stiffness parameters are connected as follows: $k_{1,\text{y}} = 0.1E; k_{1,\text{x}} = k_{1,\text{z}} = 0.9E$. This is only an assumption, therefore, in the appendix there is a numerical study of the influence of the magnitude of $k_{1,\text{y}}/E$ within the range of 1%–40% (Fig. A·4). It can be concluded from this figure that the deformation remains comparable, regardless of the magnitude of $k_{1,\text{y}}/E$ within this

Table II. Material parameters for the membrane material model.

Material parameters		Ionomer	Reinforcement
Young's modulus E in MPa	$\text{E}_{\text{dry\_23 °C}}$	265	8840
	$\text{E}_{\text{wet\_23 °C}}$	225	6950
	$\text{E}_{\text{wet\_60 °C}}$	80	4950
Poisson's ratio ν		0.35	0.39
Initial yield stress σ_{ys0} in MPa	$\sigma_{\text{ys0\_dry\_23 °C}}$	47	320
	$\sigma_{\text{ys0\_wet\_23 °C}}$	41	300
	$\sigma_{\text{ys0\_wet\_60 °C}}$	20	250
Isotropic tangent modulus E_{Tiso} in MPa	$\text{E}_{\text{dry\_23 °C}}$	5.5	750
	$\text{E}_{\text{wet\_23 °C}}$	4.7	630
	$\text{E}_{\text{wet\_60 °C}}$	2.5	460
Coefficient of thermal expansion α in K^{-1}		1.23e-4	50e-6
Coefficient of hygroscopic β_h swelling in -	$\beta_{\text{h\_23 °C}}$	0.0852	—
	$\beta_{\text{h\_60 °C}}$	0.1258	

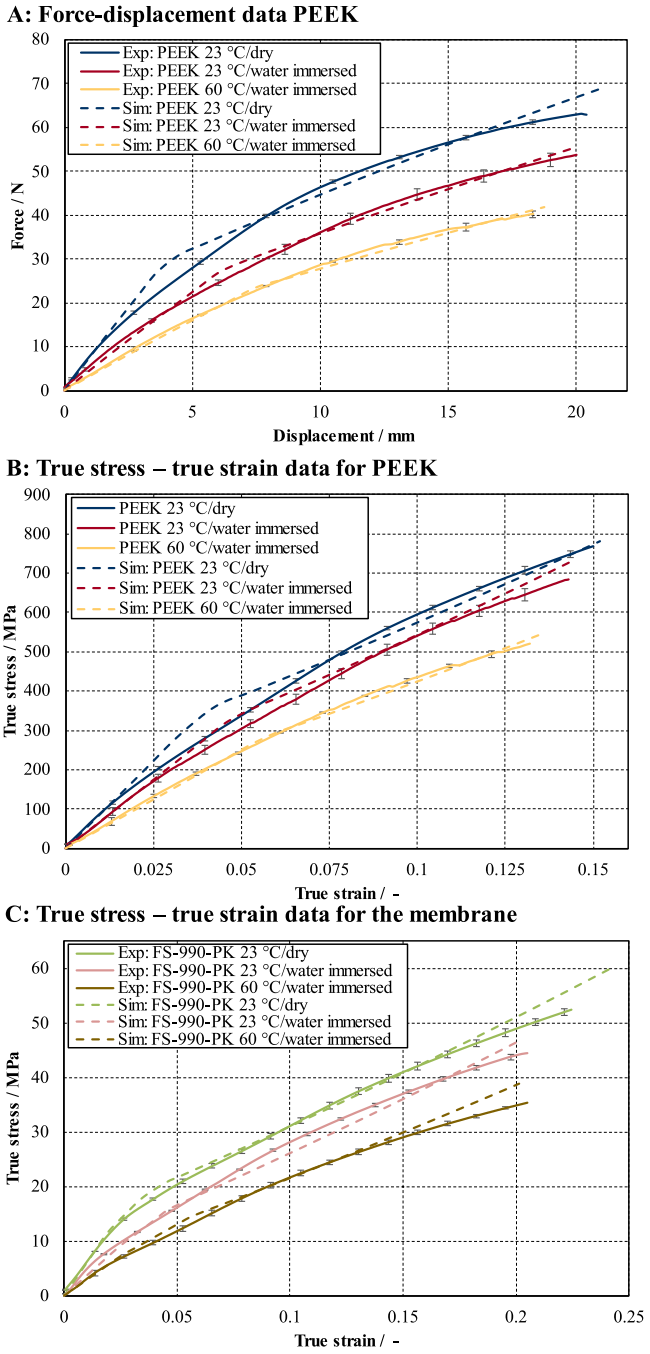

Figure 5. Comparison of the experimental and simulated data from tensile tests. A: force-displacement for the reinforcement layer (PEEK) B: true stress-true strain data (PEEK) C: true stress-true strain data (membrane).

range. However, the von-Mises stress is higher for small $k_{1,y}$ values and decreasing with increasing $k_{1,y}$. This is as expected, because the load distributes in only two directions instead of three in the case of $\frac{k_{1,y}}{E} \ll 1$.

Similar to the ionomer material model, the reinforcement layer undergoes plastic deformation at a certain stress value. The implementation follows Eqs. 10 to 15. Additionally, the fibers expand when the temperature rises, which is calculated with Eq. 16.

With both material models for the ionomer and the reinforcement layer, the tensile test simulation (Fig. 4) can be calculated, and the material parameters can be estimated. The material parameters presented in Table II were determined in a manual parameterization procedure. Between the different conditions given in Table II, a linear interpolation is applied.

Table III. Critical strain energy density values in MJ/m^3 for the materials used in the membrane under tensile loading.

Environment	PEEK	Ionomer[a)]
23 °C, 30% RH	62.1	0.41
23 °C, wet	71	0.48
60 °C, wet	74	0.55

a) The ionomer is only destroyed in the experimental tensile test after failure of the PEEK fibers, it is not expected to fail at the strain energy densities given above.

These material parameters used in the tensile test simulation (Table II and Fig. 4) lead to the results shown in Fig. 5. In Fig. 5A the comparison of the experimental and the simulated force-displacement data regarding the reinforcement layer is presented. For the three different conditions, the results are matching, and the deviations between experimental and simulated data are small. In Figs. 5B and 5C the results of the reinforcement layer and the membrane are shown in terms of true stress-true strain diagrams. In these diagrams, it is also visible that the material models match the experimental data including the large strains and the temperature and water dependence effects.

In Table III, the maximum strain energy densities from the tensile test simulations are plotted. The values are collected at the strain where the membrane failed during the experimental test. Hence, these values can be used as an indicator for failure when strain energy densities are exceeding these values in a simulation setup. It should be noted, that when the reinforcement layer cracks in the experiment, all the load is shifted immediately to the ionomer in the location of the reinforcement layer failure, and the ionomer fails there, too. For its own, it is expected that the ionomer does not fail at these energy density values.

The parameterized and validated material model for the membrane can be used in the electrolyzer cell simulation model presented in the chapter *2D-Model of the PEMWE Cell*. Therefore, in the following chapter the electrolyzer cell simulation and its results are presented and discussed.

Simulation of the PEMWE Cell Setup and its Results

In this section, the simulation of the PEMWE cell setup presented in Fig. 1A is described, and its results are discussed. The necessary simplifications for the geometry were described in *chapter 2* (Figs. 1C and 2) and the used material models were parameterized in *chapter 2* and *3*. The simulations were carried out using this model setup. The simulated load cases are the assembly and operation, differential pressure, temperature and pressure variation, gap width variation and a comparison to a setup without reinforcement layer.

The results are presented either in contour plots or in tabular form, highlighting the maximum values. Four key values of particular interest are investigated and therefore explained in detail below. The primary focus of interest lies on the membrane, comprising the ionomer layers and the reinforcement layer, which is why the subsequent discussion will concentrate on these components.

The first principal stress is the highest positive stress, indicating tensile stress. Conversely, if it is negative, only compression stress is present at that point. These stress values are compared to those obtained from the experimental tensile test. Exceeding the maximum values of the experimental data serves as a crucial indicator of potential failure, as tensile stress is commonly the primary cause of failure in polymers.[44]

Next, the von-Mises stress is analyzed. This stress measurement provides a comprehensive evaluation of both tensile and shear stress.

To prevent failure, these stress values should also remain below the maximum values obtained from the experimental tensile test.

Additionally, the first principal strain, representing the highest strain caused by load conditions, is examined. By comparing these strain values with the experimental data, it is possible to determine if the deformation is in the elastic or plastic behavior of the material. Deformations resulting from tensile stress can lead to the formation of cracks,[44] so exceeding the maximum strain observed from the tensile experiment serves as an indicator for potential failure.

In addition to the stress and strain analysis, the strain energy density (SED) is of interest. The SED is a commonly used measure for predicting failure.[45–47] Particularly high local gradients in SED indicate the possibility of a crack initiation which may lead to a failure of the membrane. It is important to ensure that the SED does not exceed the calculated values obtained from the tensile test simulation at the point of failure, as it would increase the likelihood of failure.

Assembly process and normal operation.—First, the results during assembly and operation are presented (Fig. 6). The calculated load cases are presented in Table IV. Due to the fact, that there are no time-dependent effects simulated, the duration of the steps does not change the results. The time listed in Table IV and Figs. 6–8 is given for an orientation at which load case scenario the presented step is. First, the clamping of the cell is simulated (1), which means the boundaries indicated with prescribed displacement in y-direction (Fig. 1C) are moving together. In the second step, the hygroscopic swelling of the membrane is simulated (2). Afterwards, the temperature and pressure increase (3), which leads to the operating condition at t = 50 s. Afterwards, a pressure control failure is simulated with a one-sided pressure drop (4).

In Fig. 6A, the initial setup (t = 0 s) is shown. All stresses, strains and the energy densities are zero as there is no load before clamping. The resulted geometry of the cell after the clamping is depicted in Fig. 6B, where a slight increase in tensile stresses occurs. However, they remain relatively low compared to the maximum stresses observed in experimental tensile measurements (Fig. 3). Additionally, higher von-Mises stresses and increased strains are calculated, but still low levels. The SEDs are also low, with no significant local gradients. Moving to Fig. 6C, which shows the results after swelling of the ionomer (2), all values except the first principal stress of the ionomer are increased, yet they remain low. Afterwards, the pressure and temperature are increased (3) and their distributions are presented in Fig. 6D. The tensile stresses decrease in both the reinforcement layer and the ionomer. The von-Mises stresses decrease in the reinforcement while increasing in the ionomer. Strains and SED levels increase, with values for the reinforcement remaining low. The strain values for the ionomer are approximately 50% of the failure strain compared to the values of Nafion® 117.[11] The SED continues to remain low.

In the discussed setup, which represents the normal operation mode of the electrolyzer cell (Fig. 6D), the stress and strain values during normal (undisturbed) PEMWE operation are calculated. Comparing these values with the results from the experimental tensile tests (Fig. 3, no values near the failure values are found. Therefore, it can be concluded that a failure of the membrane is not to expect.

In the model setup it is described that the cell frame, O_2-PTL and H_2-PTL 1 are modeled with a small deformation approach. This approach is valid since the maximum strains are low ($\varepsilon \leqslant 0.05$).

Disturbed operation mode: differential pressure.—Additionally, the results of a pressure control failure are depicted in Fig. 6E. Such control failure would lead to the one-sided pressure drop (Δp = 7.5 bar), in the current investigation the H_2-side is chosen for a pressure failure. The results show an increase in values comparing to the normal operation mode (Fig. 6D). The maximum tensile stress in the reinforcement layer is increased by 45% to 152 MPa, the maximum tensile stress in the ionomer is increased by a factor of six to 1.1 MPa. This increase in tensile stresses is expected, because of the compression of the H_2-PTL 2. The differential pressure leads to an additional compression and therefore the upper PTL (O_2-PTL) will shift in this direction which leads to an increased stress area at the gap between cell frame and H_2-PTL 2. However, these values are at 30% (reinforcement) and 2% (ionomer) of their failure stresses conducted in the tensile tests. The maximum von-Mises stress in the reinforcement layer is increased by 45% as well. Although the other values also display slight increases, they remain at relatively low levels. Consequently, this indicates that the membrane will not fail at a differential pressure of 7.5 bar.

Temperature and pressure variation in the electrolyzer cell.—In the following Table V, the results of the parametric variation of the temperature and operation pressure for the event of a pressure control failure (Table IV *step 4*) are presented. The maximum values of first principal stress (= tensile stress), von-Mises stress, first principal strain and SED are reported. It should be noted that the used material parameters were measured at room temperature and at T = 60 °C. At deviating temperatures, the material parameters are linearly interpolated respective extrapolated.

It can be observed that the maximum tensile stress is increased with increasing temperature. Comparing the values for T = 50 °C with T = 80 °C, a rise of the maximum tensile stress in the ionomer of 33% is calculated. The maximum tensile stress in the reinforcement layer is increased by 20%. The increase in these values can be explained with the thermal expansion and therefore an increased gap size between cell frame and H_2-PTL, which leads to additional tensile stress in the membrane. The maximum values of von-Mises stress, first principal strain, and SED are increasing also with temperature, but less than the first principal stress. All these values remain below the load limit. Therefore, it can be concluded that the likelihood of a membrane failure is increased when the temperature is increased, but still not likely.

Besides the temperature variation, a variation of the pressure is shown in Table V. The total pressure is increased approximately 50% to 11.5 bar. This leads during the differential pressure event to Δp = 11.5 bar. Due to the increased pressure, the resulting stresses and strains are increased. The maximum tensile stress in the ionomer is increased by a factor of 2, while the maximum von-Mises stress is increased by 10%. In the reinforcement layer the maximum tensile stress is increased by 16% and the maximum von-Mises stress is increased by 15%. This can be explained with the increased pressure and thus an increased compression of the H_2-PTL 2 during the differential pressure. This leads to a shift of the O_2-PTL, and the clamping stress on the membrane is increased. Therefore, the tensile and shear forces in the membrane are increased which leads to increased first principal stresses and von-Mises stresses. However, as in the cases before, all the stress-strain values stay below their load limit which leads to the conclusion that a failure is not likely.

Gap width variation.—Next, the results of the gap width variation are presented. In the initial setup a gap width of 0 mm was assumed, see results in Fig. 6 and Table V. In this subsection, the results for gap ranges between 0.01 mm and 1 mm are presented in Fig. 7. Again, the first principal stresses, the von-Mises stresses, the first principal strains and the strain energy densities are plotted. For readability, the color scale is changed compared to Fig. 6.

In Fig. 7A, the results for a differential pressure of Δp = 7.5 bar with the gap width of 0.01 mm are depicted. Comparing to Fig. 6E, the maximum values are not changing significantly. Also, the deformations are comparable. Moving to Fig. 7B, where the results of a gap width of 0.05 mm are figured, the stresses are increasing slightly and the distance between membrane and O_2-PTL is growing. Still, all values remain below load limits.

However, the results of the gap width 0.1 mm (Fig. 7C) show the beginning of a buckling of the membrane. The distance between

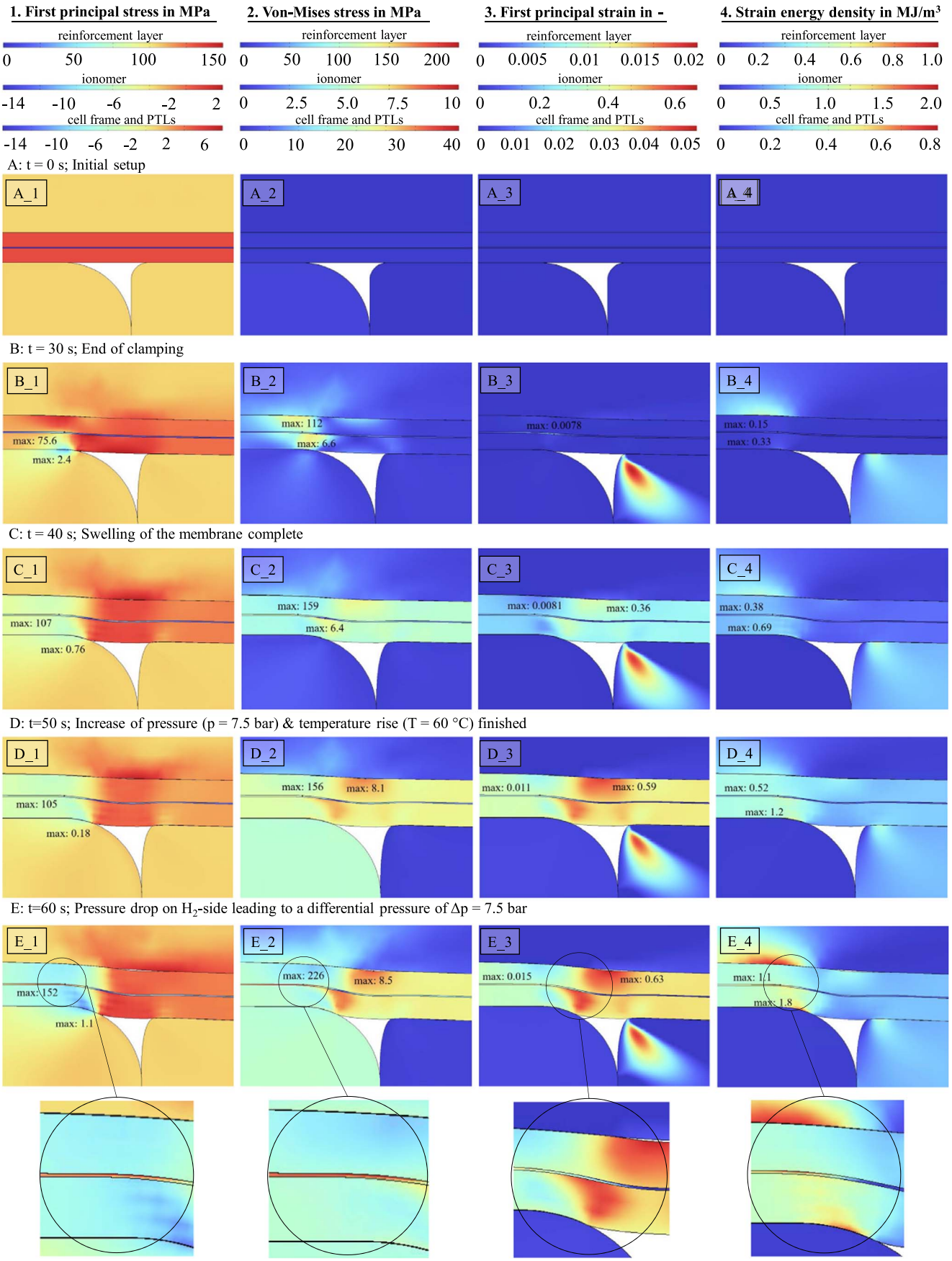

Figure 6. Stresses, strains, and strain energy densities in the cell at the gap between cell frame and H_2-PTL during assembly (A, B), operation mode (C, D) and disturbed mode (E). Example: C_3 shows the first principal strain after the swelling at t = 40 s.

Table IV. Order and duration of simulated assembly steps, operation, and pressure failure.

Number	Operational step	Time t in s
1	Clamping of cell frame and PTLs, membrane in between	0–30
2	Hygroscopic swelling of the ionomer part of the membrane	30–40
3	Temperature and pressure increase, temperature dependent hygroscopic swelling of membrane	40–50
4	One-sided pressure drop	50–60

membrane and O_2-PTL is increased, and the membrane is bent into the gap between cell frame and H_2-PTL, due to the differential pressure coming from the O_2-side. Because of that, the tensile stresses are increased, in the reinforcement from 152 MPa to 170 MPa (12%) and in the ionomer from 1.1 MPa to 3.9 MPa (354%). The increase in the ionomer by a factor 3.5 can be attributed to the bending of the membrane. Specifically, on the boundary of the membrane that is farther away from the center of the bending circle, the membrane experiences high tensile stress. On the other side of the membrane, i.e., the ionomer boundary, which is near the center of the bending circle and the folding center, the von-Mises stress as well as the first principal strain is increased (Figs. 7C_2 and 7C_3). In this area also the strain energy is increased. The values are increased, but remain under the maximum load, thus a failure is not likely.

Increasing the gap width further to 0.2 mm, the deformation of the membrane increases again and buckling occurs. The membrane buckles inside the free space in the gap between cell frame and H_2-PTL 2, which leads to increased tensile stresses in the reinforcement by a factor of 2 (307 MPa) and in the ionomer by a factor of 9 (10 MPa). Comparing to the load limits, the reinforcement layer exceeds 56% of the maximum load and the ionomer 18%. Values exceeding 50% of a failure value should be avoided to decrease the likelihood of a membrane failure. The von-Mises stress is increased to a maximum of nearly 400 MPa (Fig. 7D_2) in the reinforcement and in the ionomer to a maximum of 21 MPa. As in the pure tensile stress, the von-Mises stress in the reinforcement layer exceeds 50% of the maximum tensile stress value measured in the experimental tensile test. The strain in the ionomer exceeds the load limit of 1.18 with a maximum value of 2.3 nearly of 100%, which is an indicator of material failure at this area. Also, the SED shows a high local gradient at this point, which highlights possible failure. Therefore, it can be concluded that in this setup with a gap width of 0.2 mm a membrane failure can be expected resulting in a membrane thinning or in a possible crack initiation.

When the gap width is even more increased to 0.5 mm or 1.0 mm (Figs. 7E, 7F), the deformation and therefore the buckling of the membrane increases more. Hence, most of the stresses and strains increase even more. The folding center, especially at a gap width of 0.2 mm (Fig. 7D, is very sharp, which leads to high stress and strain peak values, which are decreasing when increasing the gap width and the following increased bending radius of the membrane.

Putting the membrane thickness d_{mem} (swollen) relative to the gap size width g_{size}, gives the following ratio:

$$r_{\mathrm{m/g}} = \frac{d_{\mathrm{mem}}}{g_{\mathrm{size}}} \qquad [22]$$

From the discussion above regarding Fig. 7, the critical gap size is between 0.1 mm and 0.2 mm. With a conservative approach, the critical membrane-gap width ratio is $r_{\mathrm{m/g}} = \frac{0.128\mathrm{mm}}{0.1\mathrm{mm}} = 1.28$. This indicates, that as long as the membrane-gap width ratio exceeds a value of 1.28, there is no buckling in the membrane and therefore the likelihood of a membrane failure is low. This can be compared to our previous work[11] using a non-reinforced Nafion®-type membrane, where, conservatively, the critical membrane-gap width ratio is $r_{\mathrm{m/g}} = \frac{0.201\mathrm{mm}}{0.2\mathrm{mm}} = 1.01$. This is a first approach to establish a limit value for the ratio of membrane thickness to gap width. This is not yet complete and must be validated by further testing. Especially, the influence of a reinforcement layer on this ratio must be determined.

Cell simulation with membrane without reinforcement layer.— As stated in the introductory text, the reinforcement woven web is non-ion conductive. This leads to higher ohmic losses in the cell, which is why the woven web should only be used if necessary. Therefore, another simulation is carried out without having an additional layer in the membrane material. So only the ionomer material parameters were used in the following results. For the comparison with the reinforcement shown in Fig. 6E, the results of the differential pressure event without reinforcement are depicted in Fig. 8. A 36% increased maximum tensile stress is calculated with the setup without the reinforcement in the ionomer, resulting in a value of 1.5 MPa. The maximum von-Mises stress is increased by 8% and the first principal strain by 10%. While the stress and strain values are increased, the maximum strain energy density decreased by 17%. The increase of the stress strain values in the ionomer can be explained by the missing support of the reinforcement layer. However, this is not an explanation for the decrease of the strain energy density. The reason for that is that the strain in this particular area is higher in the model with reinforcement.

From this follows, that the influence of the reinforcement layer in the membrane regarding mechanical stability cannot be denied but is not as high as expected. Only the maximum tensile stress can be reduced significantly using a reinforcement layer within the membrane. Hence, an immediate failure when using a non-reinforced membrane instead of the reinforced one is not to expect. Nevertheless, the stresses and strains in the membrane are higher without reinforcement, therefore the possibility of creep and membrane thinning up to crack initiation during the lifetime of the membrane is increased.

Conclusions

A structural mechanics investigation of PEMWE woven web reinforced membranes is presented in this paper with a special focus on the cell edge region, particularly at the intersection of the membrane with cell frame and the edge of the H_2-PTL. This membrane location is identified as especially critical for mechanical failures. For this purpose, experimental investigations of a representative fumasep® FS-990-PK membrane were conducted, including tensile tests of the membrane and reinforcement layer as well as the characterization of the swelling behavior.

Based on the experimental results, a geometrically simplified model of the membrane was proposed to simulate the PEMWE cell. This model was parameterized and validated using the experimental tensile test results, with high agreement between experimental and simulated data.

The PEMWE cell was analyzed during selected cell assembly and operation phases including clamping, membrane swelling, temperature and pressure increase, and a differential pressure event. Careful evaluation of the calculated stresses and strain energy densities showed that no membrane failure is to expect for the chosen geometry. Temperature increases up to 80 °C were found to increase stresses, strains, and strain energy densities in both the ionomer and reinforcement layer, but were not predicted to result in failure. Increased stresses, strains and strain energy densities were likewise determined at increasing pressures up to 11.5 bar. However,

Table V. Maximum values of stresses, strains and SED for the operation temperature of 50, 60, 70 and 80 °C at differential pressure of Δp = 7.5 bar/11.5 bar (pressure loss on H_2-side) at t = 60 s (for T = 60 °C see Fig. 6E).

Temperature/differential pressure	Max. first principal stress	Max. von-Mises stress	Max. first principal strain	Max. SED (strain energy density)
		Ionomer		
50 °C/7.5 bar	1.2 MPa	8.5 MPa	0.63	1.7 MJ/m^3
60 °C/7.5 bar[a)]	1.1 MPa	8.5 MPa	0.63	1.8 MJ/m^3
70 °C/7.5 bar	1.4 MPa	8.5 MPa	0.64	1.9 MJ/m^3
80 °C/7.5 bar	1.6 MPa	8.6 MPa	0.64	1.9 MJ/m^3
60 °C/11.5 bar	2.3 MPa	9.4 MPa	0.67	2.0 MJ/m^3
Load limit[b)] (60 °C, wet)	≈55 MPa	—	≈1.13	≈12.2 MJ/m^3
		Reinforcement layer		
50 °C/7.5 bar	147 MPa	219 MPa	0.015	1.0 MJ/m^3
60 °C/7.5 bar[a)]	152 MPa	226 MPa	0.015	1.1 MJ/m^3
70 °C/7.5 bar	156 MPa	233 MPa	0.016	1.2 MJ/m^3
80 °C/7.5 bar	161 MPa	240 MPa	0.016	1.2 MJ/m^3
60 °C/11.5 bar	176 MPa	259 MPa	0.021	1.5 MJ/m^3
Load limit (60 °C, wet)	≈550 MPa	—	≈0.2	≈74 MJ/m^3

a) Reference. b) Since the data for the ionomer in the fumasep® FS-990-PK membrane are not available, the experimental data of N117 are taken as a comparison.[11]

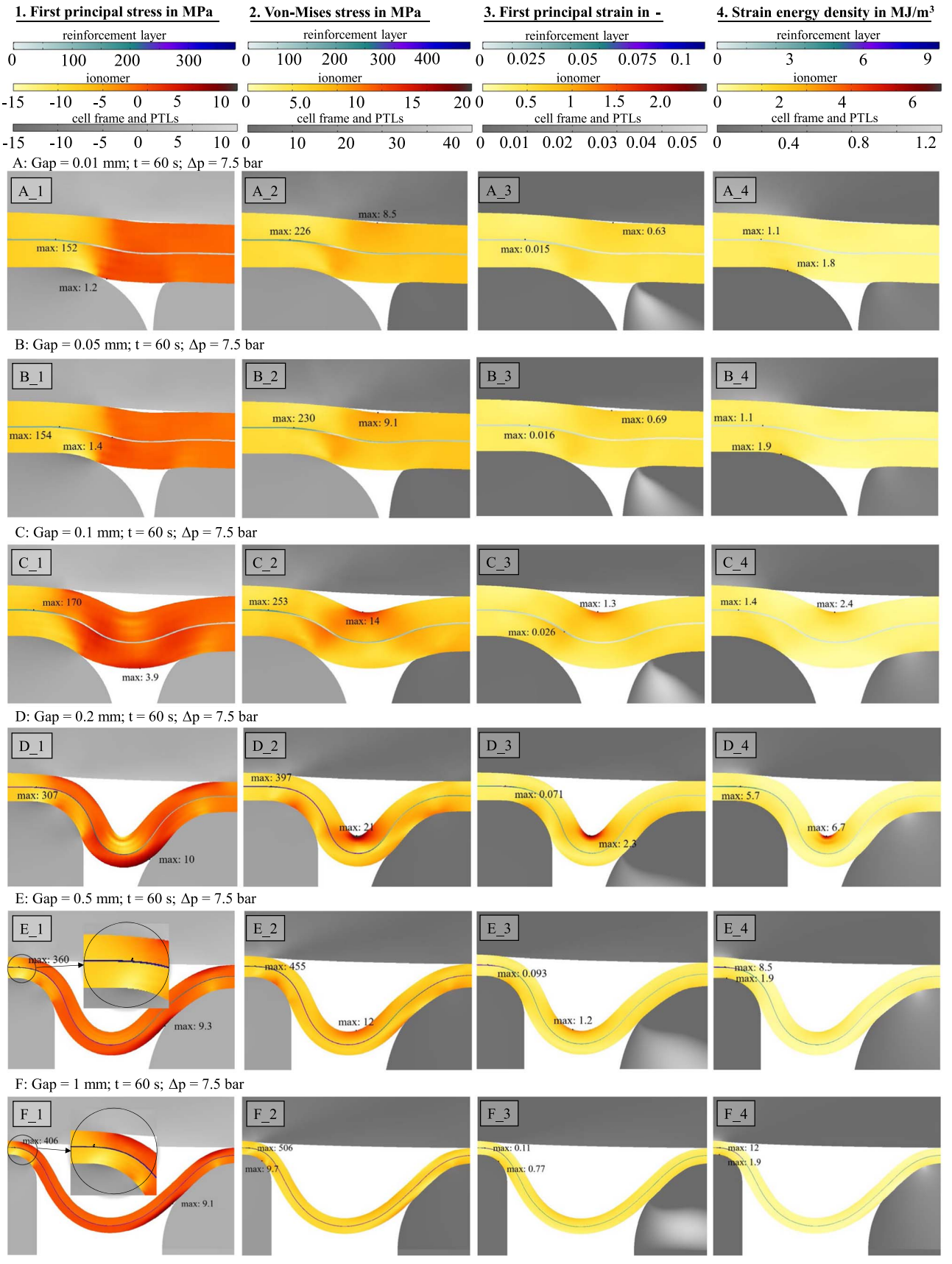

Figure 7. Results of the parameterization of the gap size between cell frame and H_2-PTL.

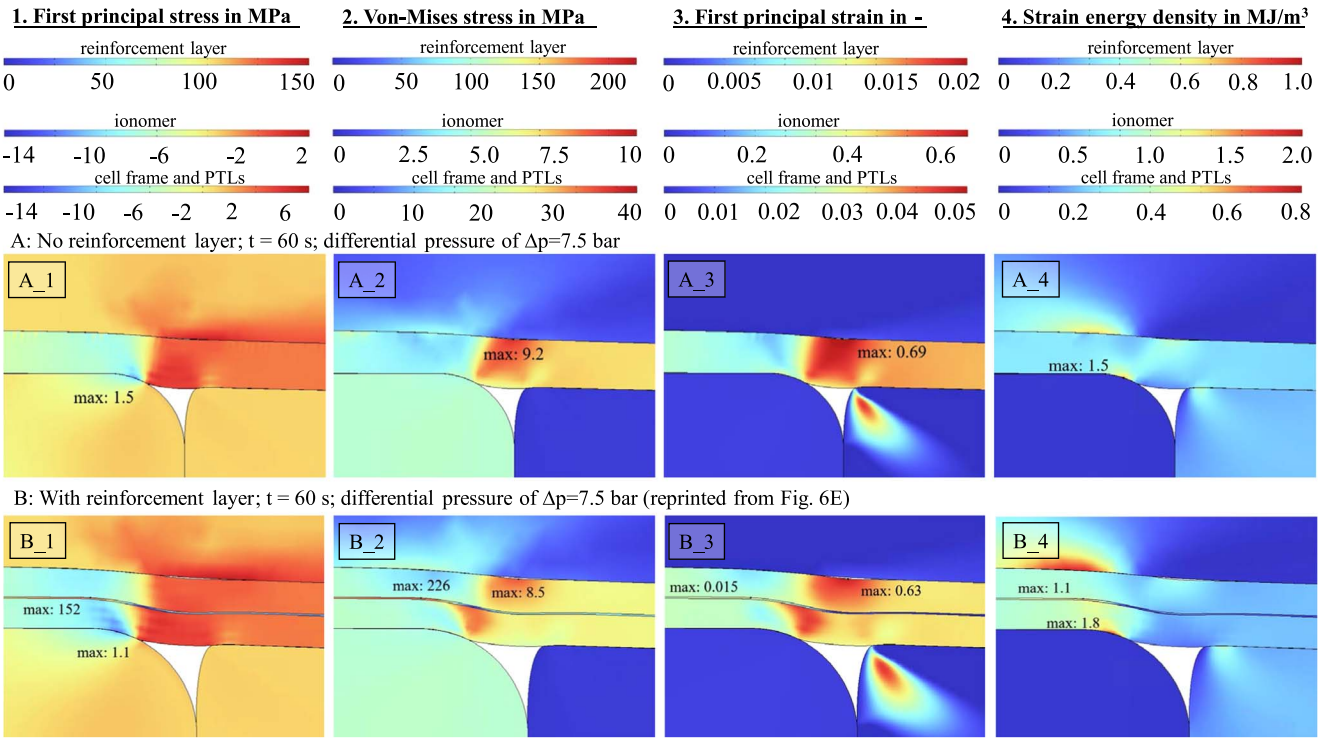

Figure 8. Stresses, strains, and strain energy densities in the cell at the gap between cell frame and PTL; A: without reinforcement layer; B: with reinforcement layer.

these values remain low compared to the maximum values observed in the experimental membrane tensile tests.

Furthermore, a parametric study of the gap width between cell frame and H_2-PTL was conducted, revealing a critical gap width of 0.1 mm at which membrane buckling begins, causing an increased likelihood of membrane failure. Increasing the gap width further resulted in significant membrane deformation, with tensile stresses of the reinforcement layer exceeding 50% of the expected maximum value and first principal strains of the ionomer locally exceeding the maximum value found in experimental membrane tests by almost 100%, indicating a high risk of membrane failure.

To determine the effect of the reinforcement layer, a simulation without this layer was performed. It was found that the reinforcement layer enhances the mechanical membrane stability, particularly in terms of maximum tensile stress, thereby increasing the expected membrane lifetime.

Further investigations are required to examine the differences between reinforced and non-reinforced membranes, specifically regarding time-dependent mechanical properties such as creep. Additionally, the influence of the membrane thickness to gap width ratio would be an interesting focus of future research. In addition to woven web reinforcement, other reinforcement techniques such as ePTFE layers are possible and should be analyzed and evaluated regarding their mechanical properties.

Acknowledgments

The publication of this article was funded by the Open Access Fund of Leibniz Universität Hannover. The authors gratefully acknowledge financial support of the German BMBF within the DERIEL project (grant numbers 03HY122A and 03HY122G).

Appendix

Governing equations for structural mechanics (reproduced from Kink[11]).—The governing equation for structural mechanics is the momentum balance in integral form, see Eq. A·1.[34] It states that the time derivative of the momentum in the volume V is equal to the sum of the surface and the volume forces acting on the volume V. Applying the Gauss' integral theorem[34] and using the second Piola-Kirchhoff stress tensor S_{PK}, Eq. A·1 can be reformulated in a differential form to Eq. A·2,[32] which is implemented into COMSOL Multiphysics®.

$$\frac{d}{dt}\iiint_V \rho\vec{v}\,dV = \iint_S \sigma\vec{n}\,dS + \iiint_V \vec{f}\,dV \qquad [A\cdot1]$$

$$\frac{\partial}{\partial t}\left(\rho^*\frac{\partial}{\partial t}\vec{u}\right) = \nabla\cdot(FS_{PK})^T + \vec{f} \qquad [A\cdot2]$$

With:

- $\rho\vec{v}$ momentum density
- $\vec{f}$ volume force density
- σ stress
- $\vec{n}$ normal direction
- V volume
- S surface
- ρ density
- $\vec{u}$ displacement
- F deformation gradient
- S_{PK} second Piola-Kirchhoff stress tensor

With the assumption of a quasistatic simulation, all time derivatives become zero. Thus, Eq. A·2 simplifies to Eq. A·3.[32]

$$0 = \nabla\cdot(FS_{PK})^T + \vec{f} \qquad [A\cdot3]$$

The deformation gradient F can be calculated with Eq. A·4, with I_d being the identity matrix. It can be multiplicative decomposed into an elastic and inelastic part, as it can be seen in Eq. A·5.[32]

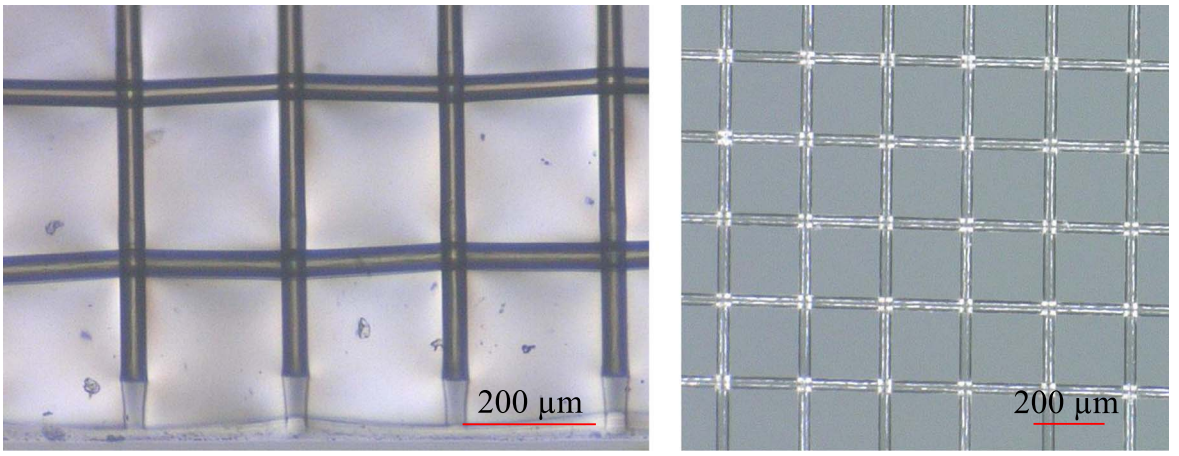

Figure A·1. left: microscopic picture of the membrane fumasep® FS-990-PK from FUMATECH; right: woven web reinforcement used in the membrane.

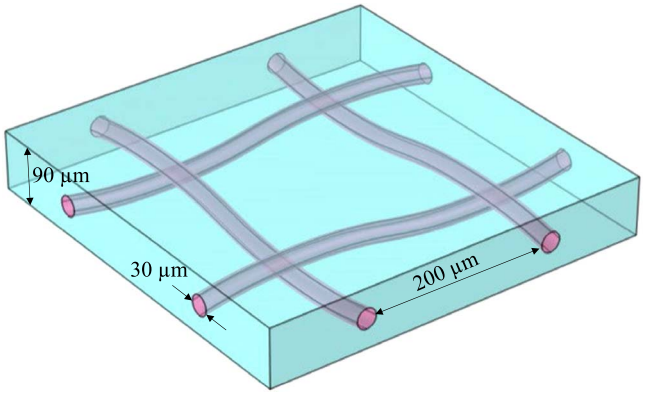

Figure A·2. Schematic[26] of the membrane fumasep® FS-990-PK from FUMATECH.

$$F = \nabla u + \mathrm{I_d} \qquad [A\cdot4]$$

$$F = F_{\mathrm{el}} \quad F_{\mathrm{inel}} \qquad [A\cdot5]$$

The deformation gradient is used for the definition of the elastic Green-Lagrange strain tensor $E_{\mathrm{GL,el}}$, see Eq. A·6.

$$E_{GL,el} = \quad \frac{1}{2}(F_{el}^{T} \quad F_{el} - I_d) \qquad [A\cdot6]$$

The second Piola-Kirchhoff stress tensor S_{PK} is a function of elastic strain energy density $W_{s,el}$, differentiated with respect to $C_{\mathrm{el}} = F_{\mathrm{el}}^{T} \quad F_{\mathrm{el}}$, see Eq. A·7.[32]

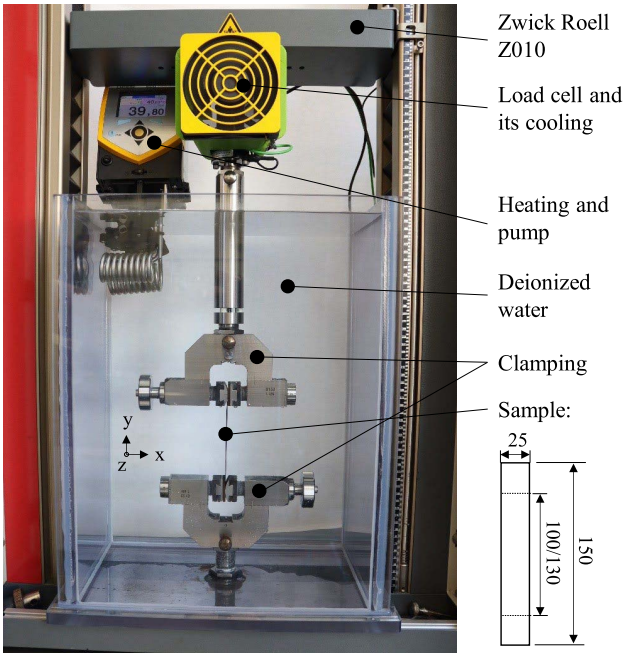

Figure A·3. Experimental setup for tensile tests and sample dimensions (in mm) according to DIN EN ISO 527–3,[11] reproduced from Kink.[11]

$$S_{PK} = \frac{\partial W_{s,el}}{\partial E_{GL,el}} = 2\frac{\partial W_{s,el}}{\partial C_{el}} \qquad [A\cdot7]$$

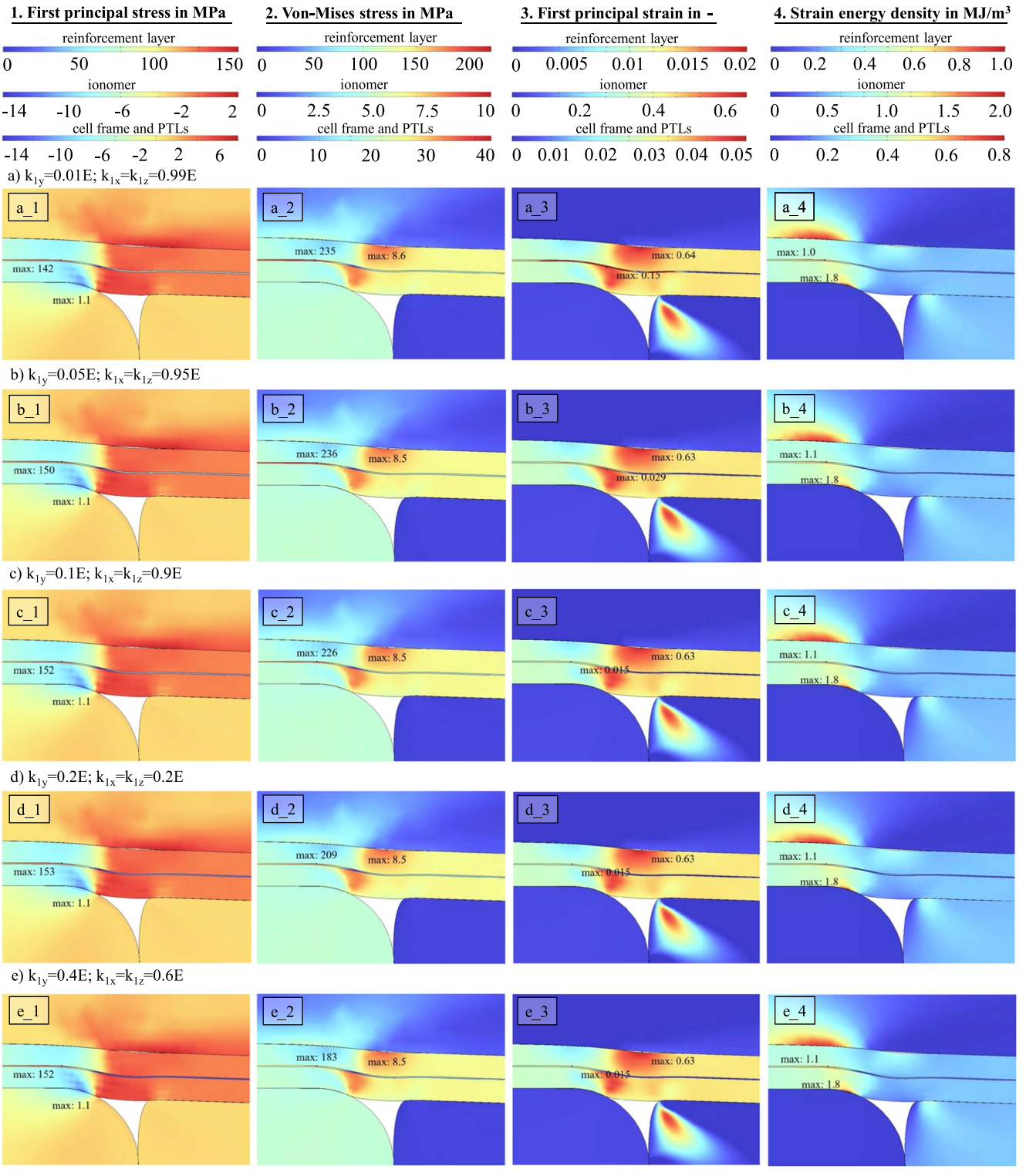

Figure A·4. Parametric study of the influence of the fiber fraction working in y-direction.

ORCID

Julian Kink https://orcid.org/0000-0002-1432-5485
Boris Bensmann https://orcid.org/0000-0001-8685-7192
Richard Hanke-Rauschenbach https://orcid.org/0000-0002-1958-307X

References

1. T. Smolinka and J. Garche, *Electrochemical Power Sources: Fundamentals, Systems, and Applications* (Elsevier, Amsterdam) (2022).
2. A. Kusoglu and A. Z. Weber, *Chem. Rev.*, **117**, 987 (2017).
3. Y. Singh, R. T. White, M. Najm, A. Boswell, F. P. Orfino, M. Dutta, and E. Kjeang, *J. Electrochem. Soc.*, **168**, 34521 (2021).
4. R. Khorasany, Y. Singh, A. Sadeghi Alavijeh, E. Kjeang, G. G. Wang, and R. Rajapakse, *Int. J. Hydrogen Energy*, **41**, 8992 (2016).
5. Y. Xing, H. Li, and G. Avgouropoulos, *Materials (Basel, Switzerland)*, **14**, 2591. (2021).
6. Y. Chen, Y. Singh, D. Ramani, F. P. Orfino, M. Dutta, and E. Kjeang, *J. Power Sources*, **520**, 230674 (2022).
7. W. Liu, D. Qiu, L. Peng, P. Yi, and X. Lai, *Int. J. Energy Res.*, **44**, 8622 (2020).
8. D. Ramani, N. S. Khattra, Y. Singh, A. Mohseni-Javid, F. P. Orfino, M. Dutta, and E. Kjeang, *J. Power Sources*, **512**, 230446 (2021).
9. D. Yang, Y. Tan, B. Li, P. Ming, Q. Xiao, and C. Zhang, *Membranes*, **12**, 306 (2022).
10. S. A. Grigoriev, K. A. Dzhus, D. G. Bessarabov, and P. Millet, *Int. J. Hydrogen Energy*, **39**, 20440 (2014).
11. J. Kink, M. Ise, B. Bensmann, and R. Hanke-Rauschenbach, *J. Electrochem. Soc.*, **170**, 54507 (2023).
12. K. Scott (ed.), *Electrochemical Methods for Hydrogen Production* (Royal Society of Chemistry, Cambridge) (2020).
13. Y. Tang, A. Kusoglu, A. M. Karlsson, M. H. Santare, S. Cleghorn, and W. B. Johnson, *J. Power Sources*, **175**, 817 (2008).
14. N. S. Khattra, Z. Lu, A. M. Karlsson, M. H. Santare, F. C. Busby, and T. Schmiedel, *J. Power Sources*, **228**, 256 (2013).
15. L. Liu, Y. Xing, Y. Li, Z. Fu, Z. Li, and H. Li, *Int. J. Hydrogen Energy*, **47**, 29014 (2022).
16. W. L. Gore & Associates, Inc., *The role of an ePTFE-reinforced Polymer Electrolyte Membrane (PEM) in the Automotive Fuel Cell Market: GORE ePTFE PEM Automotive Industry*, (Elkton, USA) (2022).
17. Y. Xing, L. Liu, Z. Li, Y. Li, Z. Fu, and H. Li, *Energy Fuels*, **36**, 11177 (2022).
18. R. Sigwadi, M. S. Dhlamini, T. Mokrani, and F. Nemavhola, *Heliyon*, **5**, e02112 (2019).
19. R. Sigwadi, T. Mokrani, S. Dhlamini, and P. F. Msomi, *J. Appl. Polym. Sci.*, **138**, 49978 (2021).
20. R. Sigwadi, F. Nemavhola, S. Dhlamini, and T. Mokrani, *International Journal of Manufacturing, Materials, and Mechanical Engineering*, **8**, 54 (2018).
21. R. Plobner, A. Spies, and J. Straub, (10.06.2020), (WO 2021/018459 Al).
22. D. H. Ye, Z. G. Zhan, Y. J. Lee, Z. K. Tu, Y. Zhang, and M. Pan, *Fuel Cells*, **13**, 1205 (2013).
23. F. S. Nanadegani, E. N. Lay, and B. Sunden, *Int. J. Energy Res.*, **43**, 274 (2019).
24. R. Omrani, S. Seif Mohammadi, Y. Mafinejad, B. Paul, R. Islam, and B. Shabani, *Int. J. Energy Res.*, **1**, 1 (2019).
25. K.-J. Bathe, *Finite Element Procedures* (Prentice-Hall, Englewood Cliffs, N.J) (2014).
26. *COMSOL Multiphysics® v. 6.1* (COMSOL AB, Stockholm, Sweden) (2023).
27. DIN Deutsches Institut für Normung e.V., Kunststoffe—Bestimmung der Zugeigenschaften—Teil 1: Allgemeine Grundsätze (ISO 527-1:2019); Deutsche Fassung EN ISO 527-1:2019 (December 2019) (2019).
28. DIN Deutsches Institut für Normung e.V., Kunststoffe - Bestimmung der Zugeigenschaften - Teil 3: Prüfbedingungen für Folien und Tafeln (ISO 527-3:2018); Deutsche Fassung EN ISO 527-3:2018 (February 2019) (2019).
29. C. Gebhardt, *Praxisbuch FEM mit ANSYS Workbench* (Carl Hanser Verlag GmbH & Co. KG, München) (2014).
30. J. Rösler, H. Harders, and M. Bäker, *Mechanisches Verhalten der Werkstoffe* (Teubner, Wiesbaden) (2006).
31. König GmbH Kunststoffprodukte, *PEEK - Polyetheretherketon: Technisches Datenblatt* (Gilching, Germany) (2016).
32. *Structural Mechanics Module User's Guide: COMSOL Multiphysics® v. 6.1* (Stockholm, Sweden)(COMSOL) (2022).
33. M. N. Silberstein and M. C. Boyce, *J. Power Sources*, **195**, 5692 (2010).
34. J. Betten, *Kontinuumsmechanik: Elastisches und inelastisches Verhalten isotroper und anisotroper Stoffe* (Springer, Berlin, Heidelberg) (2001).
35. A. Bertram, *Elasticity and Plasticity of Large Deformations: An Introduction, Second Edition* (Springer, Berlin Heidelberg) (2008).
36. Y. I. Dimitrienko, *Nonlinear Continuum Mechanics and Large Inelastic Deformations: Solid Mechanics and Its Applications* (Springer, Heidelberg) (2011).
37. G. Alberti, R. Narducci, and M. Sganappa, *J. Power Sources*, **178**, 575 (2008).
38. A. Kusoglu, B. L. Kienitz, and A. Z. Weber, *J. Electrochem. Soc.*, **158**, B1504 (2011).
39. E. Borgardt, *Schriften des Forschungszentrums Jülich, Reihe Energie & Umwelt/ Energy & Environment Band/*, **533**, 1 (2020).
40. FUMATECH BWT GmbH, *Fumasep(R) FS-990-PK: Technical Data Sheet - fumasep(R) FS-990-PK*, (Bietigheim-Bissingen/Germany) (2023).
41. G. Holzapfel, T. Gasser, and R. Ogden, *J. Elast.*, **61**, 1 (2000).
42. G. A. Holzapfel and R. W. Ogden, *Proc. R. Soc. A*, **466**, 1551 (2010).
43. T. C. Gasser, R. W. Ogden, and G. A. Holzapfel, *J. R. Soc. Interface*, **3**, 15 (2006).
44. G. Menges, E. Haberstroh, W. Michaeli, and E. Schmachtenberg, *Menges Werkstoffkunde Kunststoffe* (Munich, Germany)(Hansen) (2011).
45. P. Junker, S. Schwarz, D. R. Jantos, and K. Hackl, *Int J Mult Comp Eng*, **17**, 151 (2019).
46. P. Junker, J. Riesselmann, and D. Balzani, *Int. J. Numer. Meth. Engng*, **123**, 774 (2022).
47. J. Z. Zuo, A. T. Kermanidis, and S. G. Pantelakis, *Theor. Appl. Fract. Mech.*, **38**, 37 (2002).